



SUBJECT AREAS:
IMAGING
BIOPHYSICS
BIOPHOTONICS
APPLIED PHYSICS

Received
20 March 2012

Accepted
11 September 2012

Published
25 September 2012

Correspondence and
requests for materials
should be addressed to
P.P.M. (partha@isu.
iisc.ernet.in)

Spatial Filter Based Bessel-Like Beam for Improved Penetration Depth Imaging in Fluorescence Microscopy

Subhajit B. Purnapatra, Sampa Bera & Partha Pratim Mondal

Nanobioimaging Laboratory, Department of Instrumentation and Applied Physics, Indian Institute of Science, Bangalore 560012, India.

Monitoring and visualizing specimens at a large penetration depth is a challenge. At depths of hundreds of microns, several physical effects (such as, scattering, PSF distortion and noise) deteriorate the image quality and prohibit a detailed study of key biological phenomena. In this study, we use a Bessel-like beam in-conjugation with an orthogonal detection system to achieve depth imaging. A Bessel-like penetrating diffractionless beam is generated by engineering the back-aperture of the excitation objective. The proposed excitation scheme allows continuous scanning by simply translating the detection PSF. This type of imaging system is beneficial for obtaining depth information from any desired specimen layer, including nano-particle tracking in thick tissue. As demonstrated by imaging the fluorescent polymer-tagged- CaCO_3 particles and yeast cells in a tissue-like gel-matrix, the system offers a penetration depth that extends up to 650 μm . This achievement will advance the field of fluorescence imaging and deep nano-particle tracking.

Fluorescence imaging techniques have dramatically changed biology and medicine. Recently, it was proved beyond a doubt that, fluorescence imaging techniques are capable of going beyond the classical resolution limit¹, thereby revealing molecular dynamics with nanoscale resolution. Broadly, these super-resolution techniques may be categorized based on either point spread function (PSF) engineering or photophysical properties of the molecule. Techniques using PSF engineering include, 4PI²⁻³, stimulated emission depletion (STED) microscopy^{4,5}, aperture engineering/multiple excitation spot optical (MESO) microscopy^{6,7}, spatially structured light illumination⁸, non-linear patterned excitation microscopy⁹, and standing-wave total internal reflection fluorescence (TIRF) microscopy¹⁰ in addition to others^{11,12}. Photophysical property-based super-resolution techniques include photo-activation localization microscopy (PALM)¹³, stochastic optical reconstruction microscopy (STORM)¹⁴, fPALM¹⁵, ground-state depletion (GSDIM) microscopy¹⁶ and IML-SPIM¹⁷. Other techniques that do not belong to these categories are evanescent field-based techniques such as, TIRF^{18,19} and HILO²⁰. Notably, 3D image reconstruction in conjunction with these super-resolution techniques produce images of the highest quality^{5,21-23}. PSF engineering utilizes optical techniques, such as, interference and spatial filtering to shrink the system PSF, whereas localization techniques use photophysical phenomena, such as, photoactivation and depletion, to achieve super-resolution. The down side of these photophysical techniques is the sacrifice of temporal resolution to gain spatial resolution because these techniques collect thousands of frames to construct a single super-resolution image. Nevertheless, the contribution of some of the super-resolution techniques are noteworthy and considered to be a tool for future development. The contributions include, resolving lateral elements of the synaptonemal complex and the detection of chromosomes as twisted strings²⁴. Localization-based microscopy has revealed the clustering nature of chemotaxis receptors in the *E. Coli* cell membrane, which supports the fact that stochastic self-assembly is the cause behind periodic distribution of the receptors²⁵. The study of vesicle dynamics reveals the release of lipid probes (from granules) into the membrane without fusing thereby revealing a new mechanism^{26,27}. Multicolor TIRF microscopy is extremely useful for observing cellular dynamics near the cell membrane²⁸. Diffraction-unlimited optical data storage has been achieved with polychromatic GFP using STED imaging²⁹. A variant of STED i.e., iso-STED, was able to resolve and study the distribution of mitochondrial proteins³⁰. It was observed that, nuclear pore complexes are adjoined in peripheral and lamin heterochromatin using structured illumination microscopy³¹. There are many more studies revealing the benefits of super-resolution microscopy ranging from biology to optics. Unfortunately, the super-resolution capabilities are limited to a depth of < 150 microns, which is largely attributed to scattering in complex biological specimens.

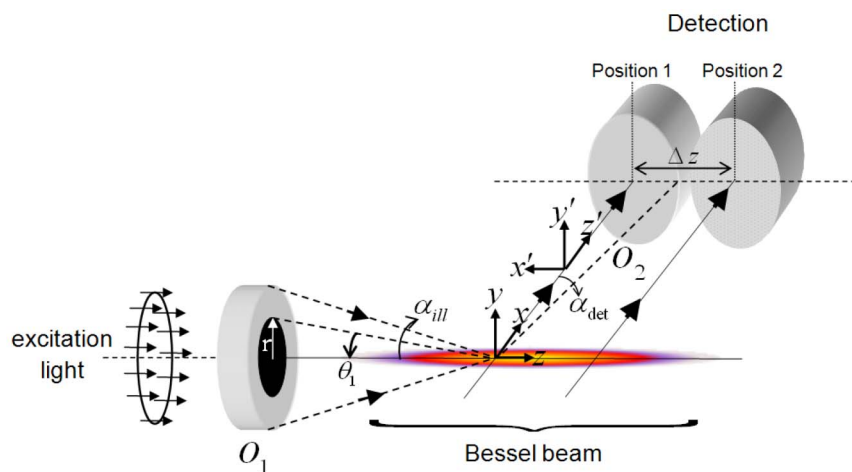


Figure 1 | Schematic diagram of the proposed imaging system, in which a Bessel-like beam illuminates the sample with theta-detection at 90° . Spatial filtering using a binary optical mask behind the illumination objective results in the generation of a Bessel-like beam. Position 1 and position 2 of the detection arm represents two different scanning positions along the optical z -axis for depth imaging.

Most of these techniques have impressive super-resolution capabilities but are limited in terms of depth imaging and suffer from poor axial resolution. Another limitation is the point-by-point-based slow scanning employed in most of the existing fluorescence imaging systems. A Bessel beam-based illumination scheme has shown promise for monitoring and imaging large specimens³². Because a pencil-like region is illuminated, the specimen is well-protected from photobleaching in comparison to confocal microscopy which illuminates the layers above and below the optical plane. We plan to lift some of these restrictions using spatial filtering techniques by employing a Bessel-like diffraction-less beam for excitation in-conjugation with theta-based orthogonal detection scheme^{33,34}. A Bessel-like excitation beam is produced by placing a binary mask at the back-aperture of the excitation objective. The generation of a Bessel-like beam using an aperture engineering technique has been reported in the literature^{35–37}. Notably, the proposed aperture engineering technique substantially reduces the ringing effect, thereby enabling fine sampling of the specimen. Reducing the ringing effect in a Bessel-like beam minimizes the background fluorescence, thereby improving the signal-to-background ratio. Such an imaging technique allows continuous scanning of specimens along the z -axis at variable depths. This technique substantially simplifies the imaging system and eliminates the need for a specialized illumination technique such as structured illumination. The advantage of the proposed technique is its simplicity and adaptability to existing imaging techniques. Specifically, this technique is well-suited for tracking functional nano-particles at greater penetration depths, enabling better understanding of complex biological processes deep inside large specimens such as, tissue, membrane and even live embryos.

Imaging deep inside thick biological tissue is severely hampered by photon scattering, which results in intensity modulations and phase mismatches. Most fluorescence imaging techniques use a Gaussian beam for illumination. The Gaussian illumination technique is well-established and useful for shallow imaging (less than 150 microns), but fails to produce quality images at larger depths (few hundreds of microns). Two-photon excitation has been specifically introduced to overcome the above drawbacks. However, the output fluorescence is severely compromised as a result of the small absorption cross-section, thereby limiting its use for fluorescence imaging³⁸. This calls for a beam that maintains its shape and size at larger penetration depths. Such a diffraction-less beam is known as a Bessel beam. It is the self-reconstruction property of the Bessel beam that maintains the profile of the beam in thick scattering specimens³⁹.

Results

In this paper, we demonstrate the generation of a Bessel-like beam and show that it can reach deep inside the sample. Another aspect of the generated Bessel-like beam is the reduction of ringing effects that enhance background fluorescence. By using an orthogonal detection system, we demonstrate the scanning capability of the imaging system with a considerable reduction in the background fluorescence. This study shows an elongated Bessel-like beam and larger penetration depths.

System PSF and its characterization. Studies were carried out to characterize the PSF of the imaging system. The excitation and emission wavelengths were chosen as 532 nm and 560 nm respectively. The schematic diagram of the proposed imaging system is shown in figure 1. The imaging system consists of two arms: the excitation arm is basically an aperture-engineered objective lens. The spatial filter belongs to the family of binary filter that allows light from the peripheral regions of the spatial filter. Spatial filtering followed by focusing using an objective lens results in a Bessel-like penetrating beam whose dimension (along the optical axis) can be tuned (by the stop angle θ_1 or equivalently by the radius r of the spatial filter) to generate a uniform field strength throughout the depth-of-focus. This technique simultaneously excites a pencil-like region encompassing all of the specimen layers and the detection system is placed orthogonal to the optical z -axis, thereby enabling quick scanning and high axial resolution. In this configuration, the axial resolution is essentially the lateral resolution of detection objective. The detection objective (O_2) can be rapidly scanned (along the optical z -axis) to obtain structural information throughout the specimen layers (see figure 1).

The system PSF at an excitation (α_{exc}) and detection (α_{det}) semi-aperture angle of 60° is shown in figure 2. The lateral XY -plane shows the ringing effects associated with Bessel beams. This effect disappears in the system PSF (XY -plane), thereby producing an ellipse-like lateral PSF. The z -profile of the Bessel-like beam (see, YZ and XZ planes) is shown in figure 2. Excitation PSF multiplied by the detection PSF results in a high resolution spot along the optical z -axis. The FWHM of the PSF along the z -axis is approximately 300 nm below the classical diffraction limit. This is impressive considering poor axial resolution of the existing fluorescence imaging system.

Depth scanning. Fast scanning at a depth of hundreds of microns is essential for obtaining vital information about a specimen. In this paper, we propose Bessel beam-based depth imaging to gain depth

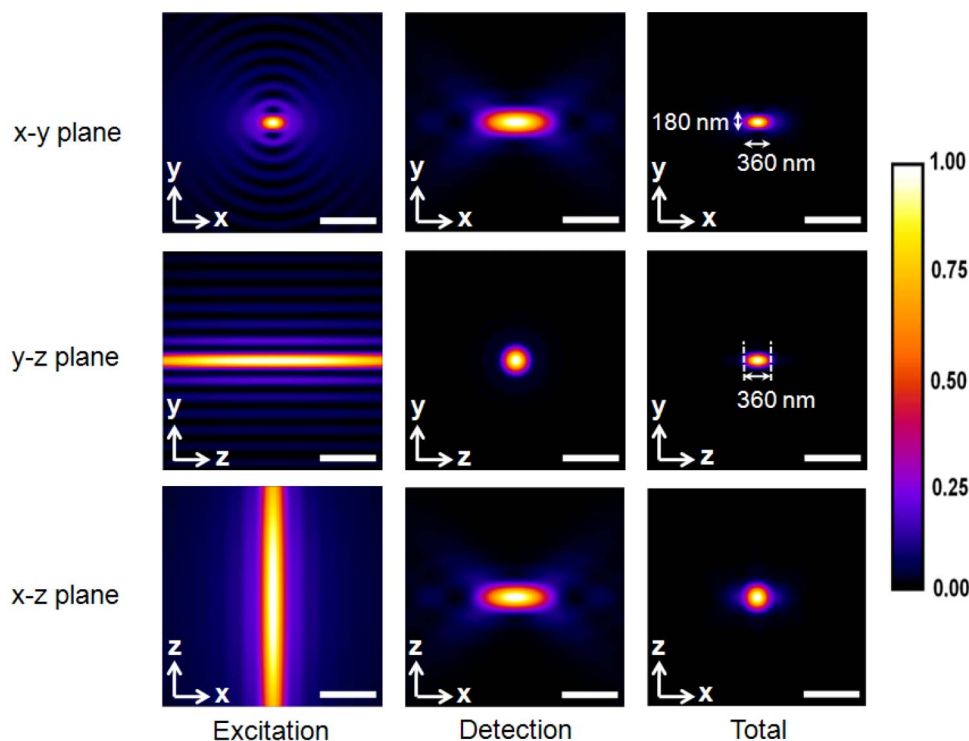


Figure 2 | The excitation, detection and system PSF at an excitation and detection aperture angle of $\alpha_{ill} = 60^\circ$ and $\alpha_{det} = 60^\circ$, respectively. Linearly polarized light of wavelength 532 nm is employed for excitation and the fluorescence is observed at a wavelength of 560 nm . The resulting axial and lateral beam profile for the generated Bessel-like beam (central lobe) along with the side rings is clearly visible. The system PSF are obtained by multiplying the excitation and detection PSFs. Scale bar = $1\ \mu\text{m}$.

information. Figure 3 shows the system PSF at various stages of the z-scanning process starting from $z = 0$ to $z = 1.92\ \mu\text{m}$. Specifically, the system PSFs are shown for $\Delta z = 0\text{ nm}$, 510 nm , and $1.47\ \mu\text{m}$. The PSF retains its shape and size throughout the scanning process along

the optical axis, but this may not be true with a real sample which is non-isotropic and causes prominent scattering. Nevertheless, this shape retention is beneficial for depth imaging applications. Because of the non-diffracting nature of Bessel-like beams, the technique may

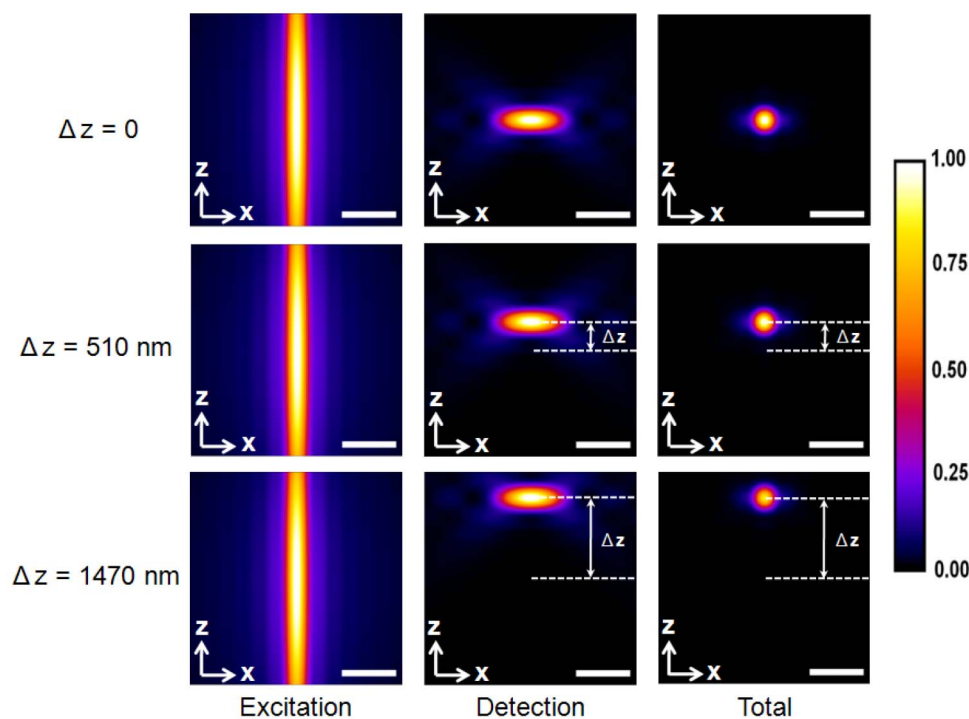


Figure 3 | The PSFs obtained by performing z-scans along the optical axis. The detection objective is scanned along the optical axis to obtain data at varying sample depths: $\Delta z = 0$, $\Delta z = 510\text{ nm}$ and $\Delta z = 1470\text{ nm}$. In this figure, Δz represents the shift from the origin as depicted schematically in Figure 1. At varying depths, the system PSF preserves its shape and size. The effects of prominent side rings are clearly minimal. Scale bar = $1\ \mu\text{m}$.

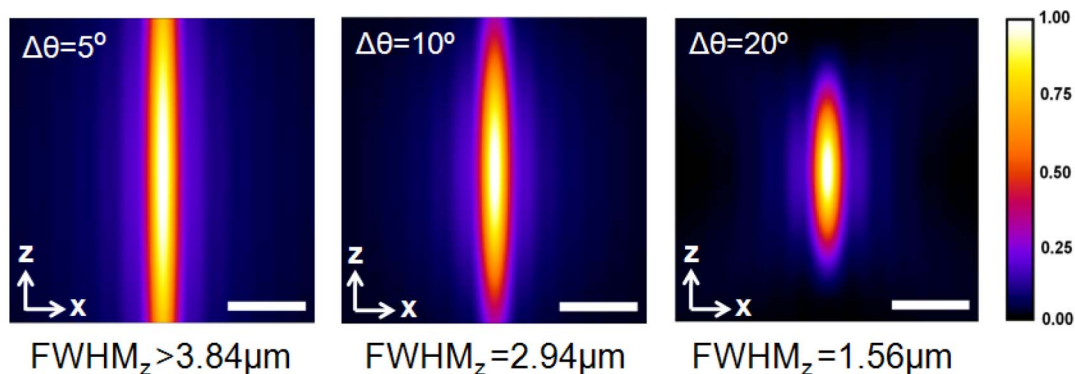


Figure 4 | PSF resizing by varying the transmission angle $\Delta\theta = \alpha - \theta_1$, where the stop angle θ_1 is determined by the spatial filter. The excitation PSF axially elongates with decrease in $\Delta\theta$ and ranges from $1.56 \mu\text{m}$ to $> 3.84 \mu\text{m}$. For large $\Delta\theta$, the excitation PSF resembles the PSF obtained using plane wave illumination. The intensities are normalized for each image. Scale bar = $1 \mu\text{m}$.

also perform well in scattering samples. However, emitted photons may undergo significant scattering as they travel through the specimen along the orthogonal direction to reach the detector. Overall, the proposed system benefits as far as high resolution depth imaging is concerned and provides the flexibility to scan the desired specimen layer. Next, we show the effect of the filter characteristics on the system PSF. Figure 4 shows the excitation PSF for varying filter stop angles. The PSF scales with the stop angle (θ_1), as the transmission window $\Delta\theta = (\alpha - \theta_1)$ is varied from 5° to 20° . The corresponding FWHM along the optical axis are $FWHM_z = 1.56 \mu\text{m}$ (for $\Delta\theta = 20^\circ$), $FWHM_z = 2.94 \mu\text{m}$ (for $\Delta\theta = 10^\circ$) and $FWHM_z \gg 3.84 \mu\text{m}$ (for $\Delta\theta = 5^\circ$). Additionally, the $FWHM_z$ becomes hundreds of microns for $\Delta\theta < 5^\circ$. Ideally, the system PSF resembles widefield PSF for small stop angles (i.e., large $\Delta\theta$), resembling full aperture uniform illumination. This scaling makes the system flexible for many biological applications that demand PSF of specific dimensions in real time, especially when imaging large biological samples such as an embryo. Finally, the polarization-dependence of the excitation PSF is analyzed. Figure 5 shows, respectively the contour plots of the excitation PSF for both x -polarized and randomly polarized light illumination. For randomly polarized light, a uniform decrease is observed in the field strength as the distance from the geometrical focus i.e. $(x, y, z) = (0, 0, 0)$ increases along the transverse plane. This uniform decrease is completely different from that of linearly polarized light illumination, which shows elliptical field

structures as the distance from the focus increases along the y -axis. The field strength does not decrease significantly along the y -axis, even as far as $1.92 \mu\text{m}$ from the geometrical focus.

Experimental results. Following the computational study, we constructed an optical system to generate a Bessel-like beam for exciting the fluorescent gel sample. The self-reconstruction property of Bessel-like beams facilitates navigations through thick and turbid media. The interference of the diffracted beam emerging from the engineered aperture mask results in the formation of Bessel-like beam. Aperture engineering has been quite successful for producing Bessel beams of desired dimension. Altering the filter parameters (aperture width $2r$ or equivalently, stop angle θ_1) of the spatial filter mask varies the size in a simple way³⁷. This adaptability is the advantage over axicon-based Bessel beam generation, where there is no tunability in the axial dimension of the Bessel beam.

The schematic diagram for obtaining the Bessel beam-based high resolution imaging is shown in figure 1. The input Gaussian beam is appropriately expanded to fill the back-aperture of the objective lens and subsequently subjected to the binary spatial filter before entering the illumination objective lens O_1 . The diffracted waves undergo constructive interference along the optical axis, thereby forming a penetrative diffraction-less Bessel-like beam. The XY , XZ and YZ planes of the Bessel beam are shown in figure 6. The measurements were taken by translating the camera that was placed directly in the

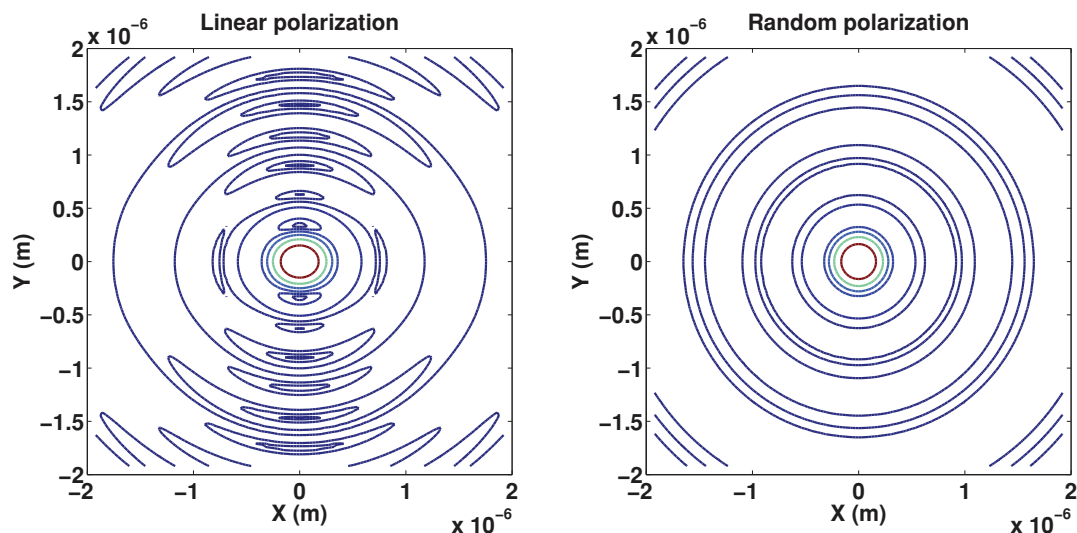


Figure 5 | Polarization effect on the excitation PSF: (a) Linearly-polarized light illumination (polarized along x -axis), and (b) Randomly polarized light illumination. The contour plots clearly show an isotropic field distribution for randomly polarized light, whereas the field has anisotropy along the y -axis.

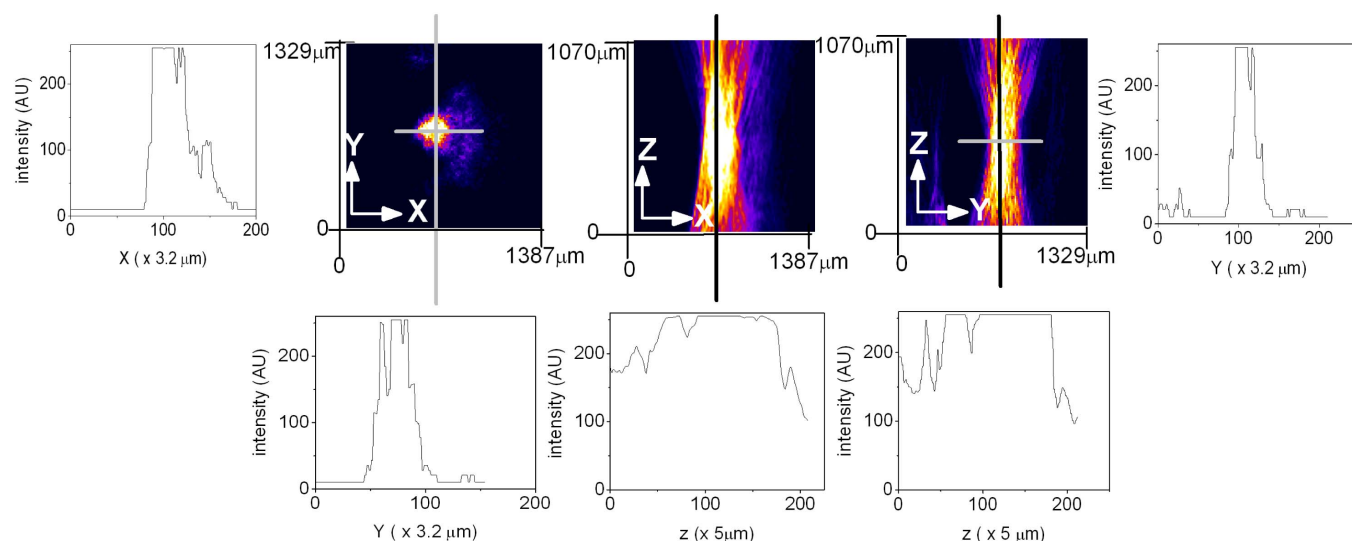


Figure 6 | Experimentally obtained illumination PSF along the XY, XZ and YZ planes showing the extended depth-of-field. A camera was placed directly in the beam path near the focal plane of the illumination objective and several images of its transverse profile were captured by repeatedly translating the camera through a known distance to obtain a 3D image. These orthogonal views are obtained from the 3D data. The Bessel beam spatially extends approximately $750 \mu\text{m}$ along the optical axis. Intensity plots are shown along the x , y and z axes for detailed visualization of the field structure at and near the focal plane. The field is uniformly stretched along the optical z -axis showing the extended depth of the Bessel beam.

beam path. The Bessel beam extends over a length of approximately $750 \mu\text{m}$ ($FWHM_z$) with a lateral (y) dimension $FWHM_y$ of approximately, $50 \mu\text{m}$. These dimensions prove that, the generated Bessel-like beam is uniform over a fairly large axial distance, which is beneficial for precise microscopy imaging and spectroscopy deep inside the specimen. Moreover, the extent of the reported beam is larger than that earlier reported in the literature³². The advantages of using the proposed spatial filter instead of axicons are the easy tunability of the Bessel beam, the depth imaging capability and the low-cost³⁷.

The detection arm consists of a separate objective for collecting the fluorescence emanating from the fluorescent gel-matrix sample (see, sample preparation section for the preparation details of the sample). The detection arm is placed at an orthogonal angle offering high numerical aperture (NA) at long working distance apart from achieving maximum elimination of incident light. After emerging from the back of objective lens O_2 , the parallel rays are then filtered using a long-pass filter (with a cut-off wavelength of 550 nm) to remove the stray light and are finally focused on to the CCD camera. It may be reminded that, the system PSF is the product of excitation PSF and the detection PSF. In this system, the excitation PSF is the diffractionless Bessel-like beam penetrating through all of the specimen layers, and the detection PSF is a dot-like structure (formed by the objective lens O_2) which is placed orthogonal to the excitation objective (see, figure 1 and figure 2). The schematic diagram (see, figure 7A) shows the translation of detection PSF along the Bessel beam, thereby scanning the specimen along the length of the excitation PSF. The corresponding contour plots of the system PSF at varying depths of the fluorescent gel matrix are shown in figure 7B. The system PSF is obtained at a depth ranging from $50 \mu\text{m}$ to almost 1 mm . This range demonstrates the incredible penetrating property of the excitation PSF. Moreover, the system PSF preserves its shape to a depth of $650 \mu\text{m}$. The axial length (measured as the FWHM along the optical axis) and lateral (along transverse y -axis) extent of the Bessel-like beam are approximately $300 \mu\text{m}$ and $25 \mu\text{m}$, respectively. The length of the Bessel beam can be varied by changing the diameter $2r$ of the spatial filter which is equivalent to changing the stop angle (θ_1). The adaptable length of Bessel-like beam which depends on the spatial filter radius (shown in figure 1) provides the tunability required for various applications in bioimaging.

We imaged coated CaCO_3 particle clusters with dimensions of $3 - 10 \mu\text{m}$ in a gel matrix. In the present experimental setup, we have used both $10X$, $NA = 0.3$ and $20X$, $NA = 0.4$ objectives. Specifically, the imaging of CaCO_3 particles in the gel-matrix were carried out using $20X$ detection objective. The images were acquired at varying depths, from which only 2 images at a depths of $108 \mu\text{m}$ and $358 \mu\text{m}$ (shown by red circles) are shown in figure 8. The zoomed image of coated CaCO_3 -cluster is also shown for visualizing the structures. The image quality is impressive at a depth of $358 \mu\text{m}$ considering the fact that the gel matrix is highly scattering. The internal structure of the CaCO_3 cluster is clearly visible even at a depth of $350 \mu\text{m}$ and thus demonstrates in-depth high resolution imaging in a scattering medium (gel-matrix). This enhanced depth is a result of the self-reconstruction property of the Bessel beam³⁹. Traces of the larger cluster are also visible in the image at position 1 (green circle) which are caused by the stray light and the large field-of-view of the detection objective.

Imaging cells deep inside a tissue-like scattering specimen is of potential interest for understanding complex biological phenomenon. In the present study, yeast cells were imaged in a tissue-like scattering gel-matrix. This type of specimen is important for assessing imaging capabilities in a scattering specimen while isolating other effects such as, auto-fluorescence and photobleaching. The yeast cells were coated with three-layers of fluorescently-tagged polymers. The coating process and sample preparation are described in Supplementary 1. Figure 9 shows the cell images at varying depths, $\Delta z = 296 \mu\text{m}$ (A), $\Delta z = 478 \mu\text{m}$ (B) and $\Delta z = 616 \mu\text{m}$ (C) (shown by the white arrow in figure 9). Similar to CaCO_3 imaging (in figure 8), traces of cells from other layers are also visible. Again, these traces are caused by stray light and the large field-of-view of the detection objective (O_2). Practically, the working distance for large NA objective ($NA > 0.4$), is usually very small (approximately few millimeters). Therefore, the optical alignment and data collection in the orthogonal detection configuration become very difficult. Moreover, the full-width half-maxima (FWHM) is calculated for several yeast samples at varying depths as shown in figure 9. The intensity plots are shown in figure 9 (D,E,F) and the corresponding FWHM is found to be $2.04 \mu\text{m}$, $2.36 \mu\text{m}$ and $2.12 \mu\text{m}$ at depths of $\Delta z = 296 \mu\text{m}$, $478 \mu\text{m}$ and $616 \mu\text{m}$ respectively. These findings reveal that, the FWHM is approximately preserved throughout the sample depth of $616 \mu\text{m}$,

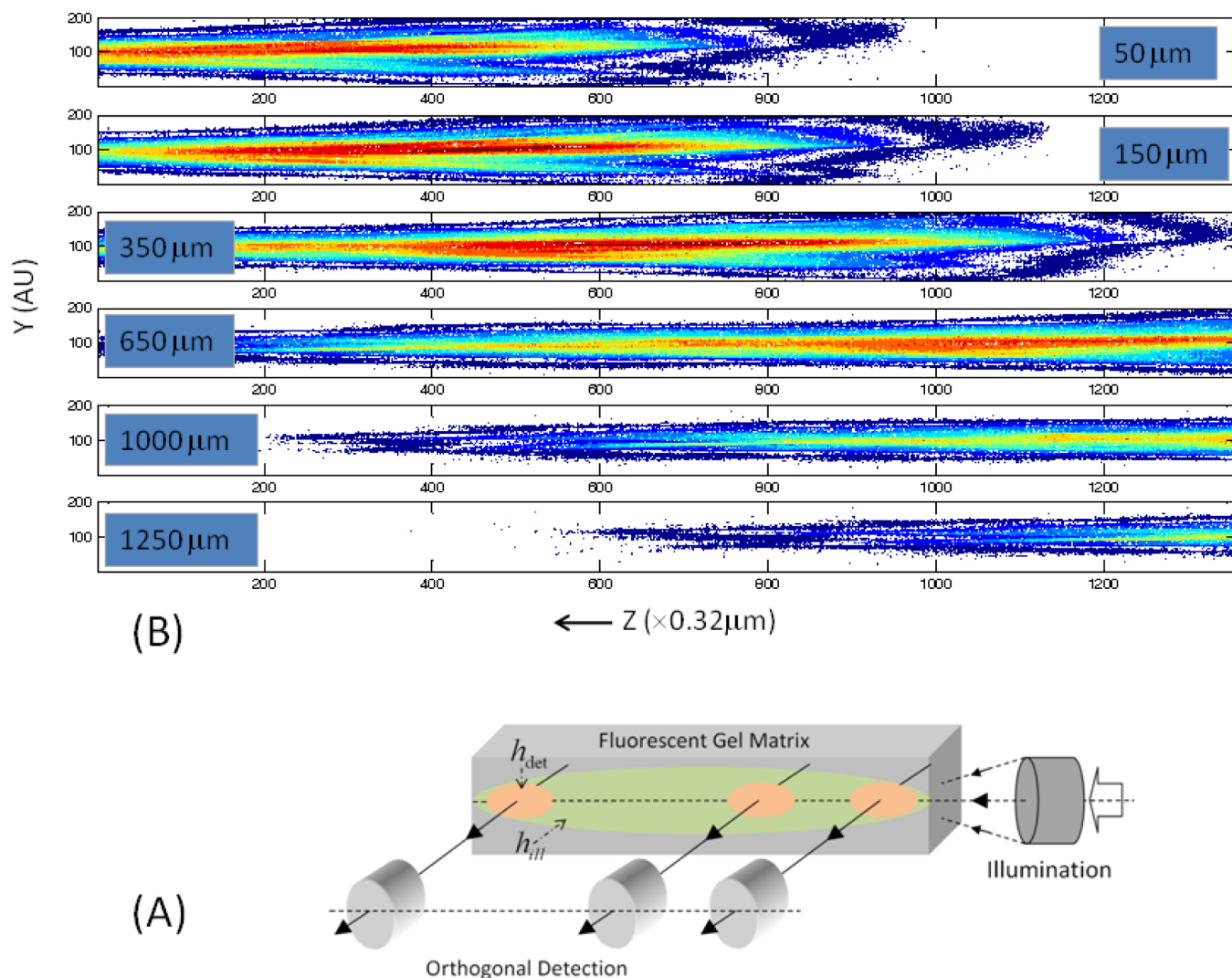


Figure 7 | (A) Cartoon showing the system PSF as it enters the fluorescent gel sample at varying z-depths along with the theta-detection geometry, (B) The experimentally obtained contour plots of the PSF at varying depth (ranging from 50 μm to 1.25 mm) of the fluorescent gel sample. The depth information is indicated on each image and denotes the distance of the right-most corner of each image from the coverslip. The depth penetration capability of the Bessel beam is quite evident.

thereby demonstrating the diffractionless property of the Bessel beam.

Finally, we performed depth-imaging studies with a state-of-art laser scanning confocal microscope (Zeiss, LSM 700) for comparison with the proposed technique. We used a confocal pinhole of 46.5 μm for obtaining the sectional images at varying specimen depths. The specimen comprised of fluorescently-coated Yeast cells engaged in a gel-matrix. Figure 10(a,b,c) shows the XY-, YZ- and ZX- sections of the specimen along with a cartoon (figure 10d) describing the imaging parameters (such as, the position of the coverslip, and the coordinates of the sample plane). From the YZ-plane (figure 10b), it is clear that the penetration depth of the confocal system is approximately 227 μm . A penetration depth of about 200 μm for a confocal system was recently reported in the literature⁴⁰. Figures 10e and 10f show the magnified image (obtained using a PLAN Neofluor 20X/0.4 NA objective lens) of the specimen at a depth of 16 μm for direct comparison with the images at a depth of 227 μm (see, inset of figure 10a). To further demonstrate the system resolution, FWHM was obtained at varying depths. At depths of 16 μm and 227 μm , the FWHM is found to be 2.29 μm and 3.15 μm respectively (see, figure 10g and 10h). The broadening of the FWHM is clearly evident, revealing the deteriorating resolution of the confocal system at

greater depths. In contrast, the proposed Bessel beam-based imaging system retains the FWHM of the system PSF at much greater depths (see, figure 9). This gives an approximate estimate of the resolution of the proposed imaging system and its comparison with the confocal system. Similar images were also obtained for another specimen (fluorescent polymer-coated CaCO_3 particles embedded in the gel-matrix) as shown in the supplementary material (see, supplementary 1, figure 4).

Discussions

The aperture engineering technique offers an efficient way of generating a Bessel-like beam and the ability to reach a depth of hundreds of microns. The diffraction-less property of the Bessel-beam makes it a natural choice for imaging scattering specimens which are otherwise inaccessible by other means of microscopy imaging techniques such as, widefield, CLSM, 4PI, structured illumination microscopy and others. Notably, the experimental results show substantial minimization of the concentric ring effect, thereby facilitating a fine scanning ability without causing undue background fluorescence.

Confocal laser scanning microscopy (CLSM), Structural illumination microscopy (SIM) and other scanning-based fluorescence imaging techniques have advanced the fields of biophysics, biophotonics and

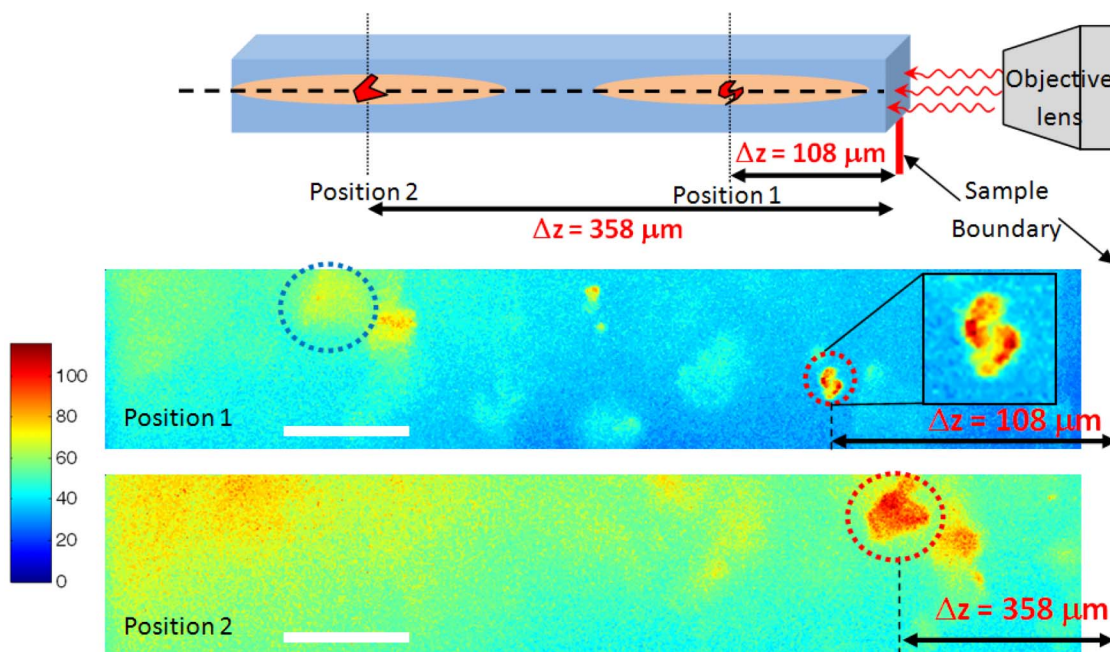


Figure 8 | Images of clusters of fluorescent polymer coated CaCO_3 particles (size 3 – 10 μm) inside a tissue-like gel matrix at depths of 108 μm , and 358 μm from the sample boundary. The location of this sample boundary is indicated by the red line and both positions 1 and 2 are located with respect to this line. A few out-of-focus clusters can be observed in position 1, one of these is encircled in blue. This same location is brought to focus by adjusting the detection arm along the optical axis (x-axis, see Figure 1.) and captured in position 2. A section in which a few coated CaCO_3 particles are clustered has been magnified. The scale bar (in white) represents 55 μm .

nanoscale imaging. However, the inability to improve the penetration depth has limited the use of these techniques in thick scattering samples such as tissue. The PSF of these imaging systems broadens at large depths in the sample, results in phase-mismatch and gives rise to poor-resolution. These effects rule out the very concept of high-resolution noise-free imaging. Widefield and CLSM imaging suffer from autofluorescence and off-layer (top and bottom of focal plane) excitation. With the improved depth penetration of Bessel-like beam, the illumination can be limited to just a pencil-like region of the specimen, thereby preventing premature photobleaching of the neighboring regions. Additionally, we observed a substantial reduction of the ringing effect surrounding the central pencil-like beam, which further reduce undue photobleaching and off-focus fluorescence. This illumination scheme coupled with orthogonal detection demonstrates the capability for selective imaging from a specific plane deep inside the specimen. In such a configuration, the lateral resolution of the illumination arm determines the axial resolution of the overall imaging system, which is beneficial for deep selective plane imaging. It is difficult to go down to a resolution of few hundreds of nanometers because of the small working distance of high NA detection objective. Nevertheless, this configuration enables the study of thick scattering biological specimens at large penetration depths.

The ability to look deeper inside a biological specimen has profound implications in biological systems. This ability is prohibited by the poor transmission of light through the specimen which comprises several interfaces and scattering centers. To increase penetration, one has to employ a beam that does not undergo significant diffraction. Specifically, the Gaussian beam is known to have significant diffraction. Bessel beams show much promise which is mainly because they are diffractionless and can self-reconstruct. When obstructed, the scattered field interferes with the unscattered field, resulting in constructive interference along the direction of beam propagation (which is same as the optical axis). Mathematically, the complex amplitude of the Bessel-like beam can be modeled as, $U(\vec{r}) = C_0 J_0(k_T \rho) e^{-jk_z z}$, for which the intensity distribution is,

$I_B = |U|^2 = |C_0|^2 J_0^2(k_T \rho)$, where, $k_T = \sqrt{k_x^2 + k_y^2}$; k_x , k_y , & k_z are the components of the wave-vector. The presence of a Bessel function in the intensity expression accounts for the side rings which decrease as $\rho = \sqrt{x^2 + y^2}$ increases and most importantly the intensity is independent of the propagation direction z , thus there is no spread of intensity. Therefore, the Bessel beam can propagate deep inside the scattering sample. In contrast, the intensity of the Gaussian beams is given by, $I_G = C_1 e^{2\rho^2/W^2(z)}$; $W(z) = W_0 \left[1 + \left(\frac{z}{z_0} \right)^2 \right]^{1/2}$ and has a z -dependence. Therefore the intensity spreads strongly at interfaces (refractive index mis-matches) in the biological specimen.

The imaging technique has demonstrated quality imaging of both functionalized nanoparticles and polymercoated yeast in a thick gel matrix. PSF distortion is inevitable at large penetration depths especially in a scattering sample. This technique demonstrates that Bessel beam-based excitation extends the imaging limit to almost 650 μm . In contrast, Gaussian beam-based excitation techniques are limited to ≈ 200 microns. Moreover, in an ideal isotropic medium, the computational study revealed that the PSF retains its shape at greater penetration depths. We have already witnessed in our gel-matrix sample that this does not hold true for $z > 650$ μm . In the computational study, scattering effects were not incorporated, which is a result of the difficulty in modeling the scattering process in a complex biological environment. The PSF undergoes substantial distortion at greater penetration depths in a realistic sample, such as the tissue-like gel-matrix sample. Therefore, we conclude that reliable imaging is possible for $z \leq 650$ μm . Within this range, the recorded images (see, figures 8 and 9) show the capability for high quality imaging. In the future, this technique will attract applications in particle tracking deep inside tissue and optical injection in addition to fluorescence imaging applications.

Methods

Excitation and detection scheme. The flexibility for obtaining information from any desired layer of the specimen is of paramount importance in fluorescence imaging.

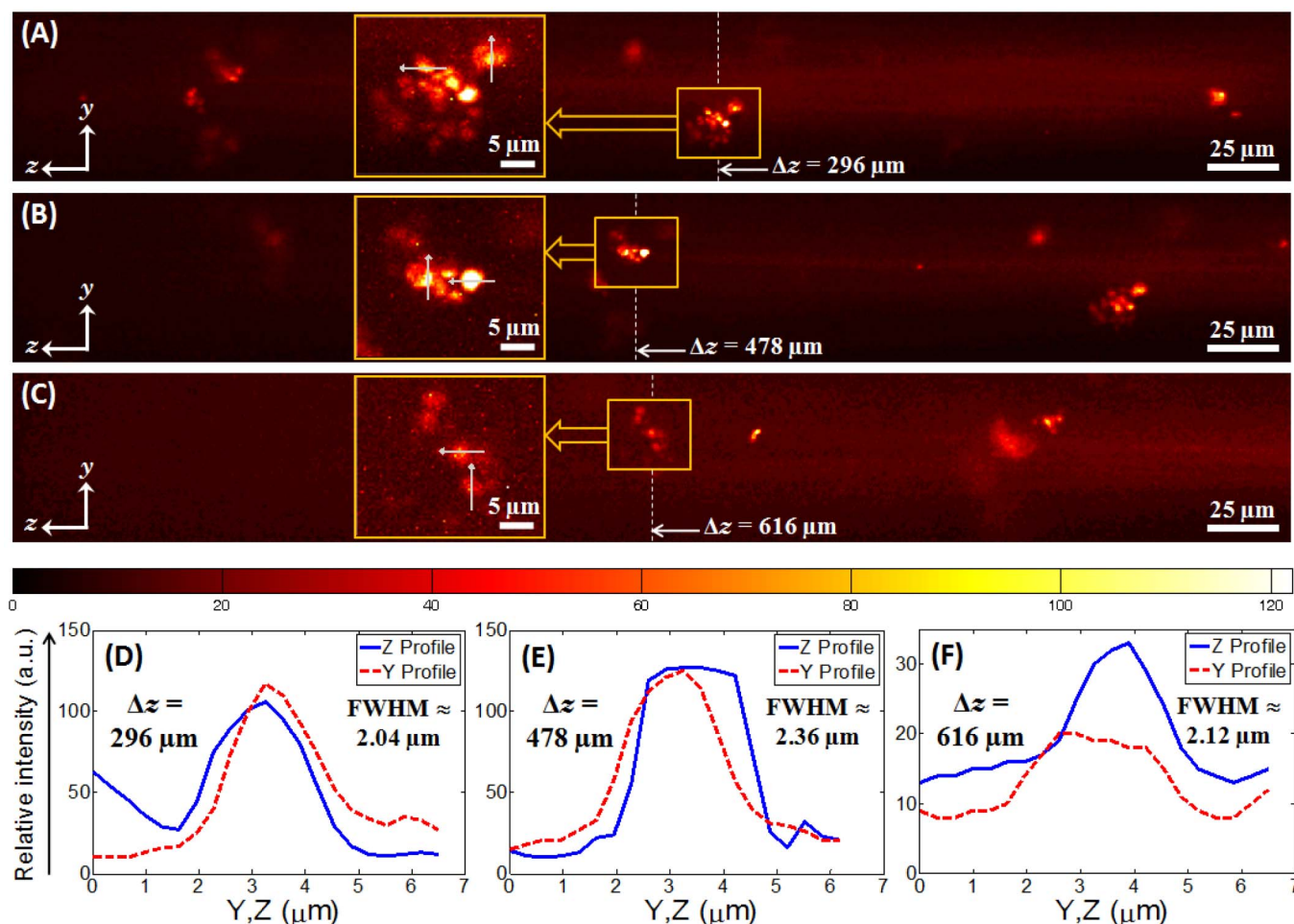


Figure 9 | Fluorescent polymer (PAH conjugated with NHS-Rhodamine dye) coated Yeast cells are uniformly distributed throughout the tissue-like gel sample. Several images were captured by translating the detection arm by $50 \mu\text{m}$; three of these images are shown here, each highlighting a prominent cluster of Yeast cells. These clusters were observed at depths of $296 \mu\text{m}$ (A), $478 \mu\text{m}$ (B), and $616 \mu\text{m}$ (C) from the coverslip. The inset shows a zoomed portion of a few clustered Yeast cells. (D), (E) and (F) are the intensity plots along the white line passing through the clusters in these inset figures of (A), (B) and (C). The FWHM values (obtained by averaging the Y and Z profile) are indicated in each intensity plot. It is evident that, the FWHM does not appreciably increase at greater penetration depths thereby supporting the fact that resolution deep inside the specimen is restored. The scale bar (in white) represents $25 \mu\text{m}$.

Assuming linearly polarized light illumination and spatial filtering techniques, the resulting electric field at the geometrical focus is given by^{41,42},

$$h_{\text{exc}}(u, v, \phi) = |\bar{E}(u, v, \Delta\theta)|^2 = |\bar{I}_0|^2 + 4|\bar{I}_1|^2 \cos^2(\phi) + |\bar{I}_2|^2 + 2\cos(2\phi) \text{Re}\bar{I}_0\bar{I}_2^* \quad (1)$$

where, the modified diffraction integrals over the aperture angle are,

$$\bar{I}_0(u, v) = \int_{\Delta\theta} M(*) (1 + \cos\theta) \sin\theta \times J_0\left(\frac{v \sin\theta}{\sin\alpha}\right) \cos^{1/2}\theta e^{i\left(\frac{u \cos\theta}{\sin^2\alpha}\right)} d\theta,$$

$$\bar{I}_1(u, v) = \int_{\Delta\theta} M(*) \sin^2\theta J_1\left(\frac{v \sin\theta}{\sin\alpha}\right) \cos^{1/2}\theta e^{i\left(\frac{u \cos\theta}{\sin^2\alpha}\right)} d\theta, \text{ and}$$

$$\bar{I}_2(u, v) = \int_{\Delta\theta} M(*) (1 - \cos\theta) \sin\theta J_2\left(\frac{v \sin\theta}{\sin\alpha}\right) \cos^{1/2}\theta e^{i\left(\frac{u \cos\theta}{\sin^2\alpha}\right)} d\theta. u, v \text{ and } \phi \text{ are}$$

the longitudinal coordinate, transverse coordinates and azimuthal angle respectively⁴². The function, $M(*) = H[\theta - \theta_1] - H[\theta - \alpha]$ represents the spatial filter, and $H[a - b] = \{0, a \leq b; 1, a > b\}$ is the Heaviside step function. θ_1 is the parameter controlling the transmission characteristics of the filter through the outermost annulus defined by $\Delta\theta = \alpha - \theta_1$ (see figure 1).

We employ confocal theta detection scheme, where the detection is performed in the orthogonal plane, as shown in figure 1. The transformation matrix representing

$$\text{the orthogonal plane is given by, } \begin{bmatrix} x' \\ y' \\ z' \end{bmatrix} = \begin{bmatrix} 0 & 0 & -1 \\ 0 & 1 & 0 \\ 1 & 0 & 0 \end{bmatrix} \begin{bmatrix} x \\ y \\ z \end{bmatrix}. \text{ This detection}$$

scheme has the advantage of high resolution at long working distances. Since, the emission process is isotropic and the fluorescent light is randomly polarized, the detection PSF is given by,

$$h_{\text{det}}(x', y', z') = |\bar{E}(x', y', z')|^2 \quad (2)$$

$$= |\bar{I}_0(x', y', z')|^2 + 2|\bar{I}_1(x', y', z')|^2 + |\bar{I}_2(x', y', z')|^2 \quad (3)$$

where the integration $I_{0,1,2} = \int_{\theta=0}^{\alpha} (\dots) d\theta$ on the aperture-free detection objective is carried over the detection aperture angle α_{det} . Overall, system PSF of the proposed imaging system is given by,

$$h_{\text{sys}}(x, y, z) = h_{\text{III}}(x, y, z) \times h_{\text{det}}(x', y', z'). \quad (4)$$

For the computational study, the excitation wavelength was chosen as 532 nm , for which the fluorescence emission was collected at 560 nm . We have chosen to work at a sampling rate (well above the Nyquist sampling rate) of 30 nm along the entire x, y , & z axes. For the simulation, the number of pixels chosen along the lateral x, y axes were 128×128 and 128 of these planes were considered along z -axis. This gave a lateral (xy) and axial (z) range of about $3.84 \times 3.84 \mu\text{m}^2$ and $3.84 \mu\text{m}$ respectively. The integration over the modified diffraction integrals, \bar{I}_0, \bar{I}_1 and \bar{I}_2 was performed over the transmission angle ($\Delta\theta$). The detection PSF is similar to the excitation PSF except for the scaling introduced by the Stokes-shifted emission wavelength of 560 nm . The detection scheme consists of scanning along the z -axis to successively collect light from different layers of the 3D specimen.

Generation and characterization of a Bessel-like beam. To generate a Bessel beam, we used aperture engineering techniques. A special optical binary mask was employed that allows the light to pass through the outermost annular region (see, Supplementary 2). This structured light is then allowed to pass through the back-aperture of the objective lens. The spatial filter has a radius of 12 mm and is

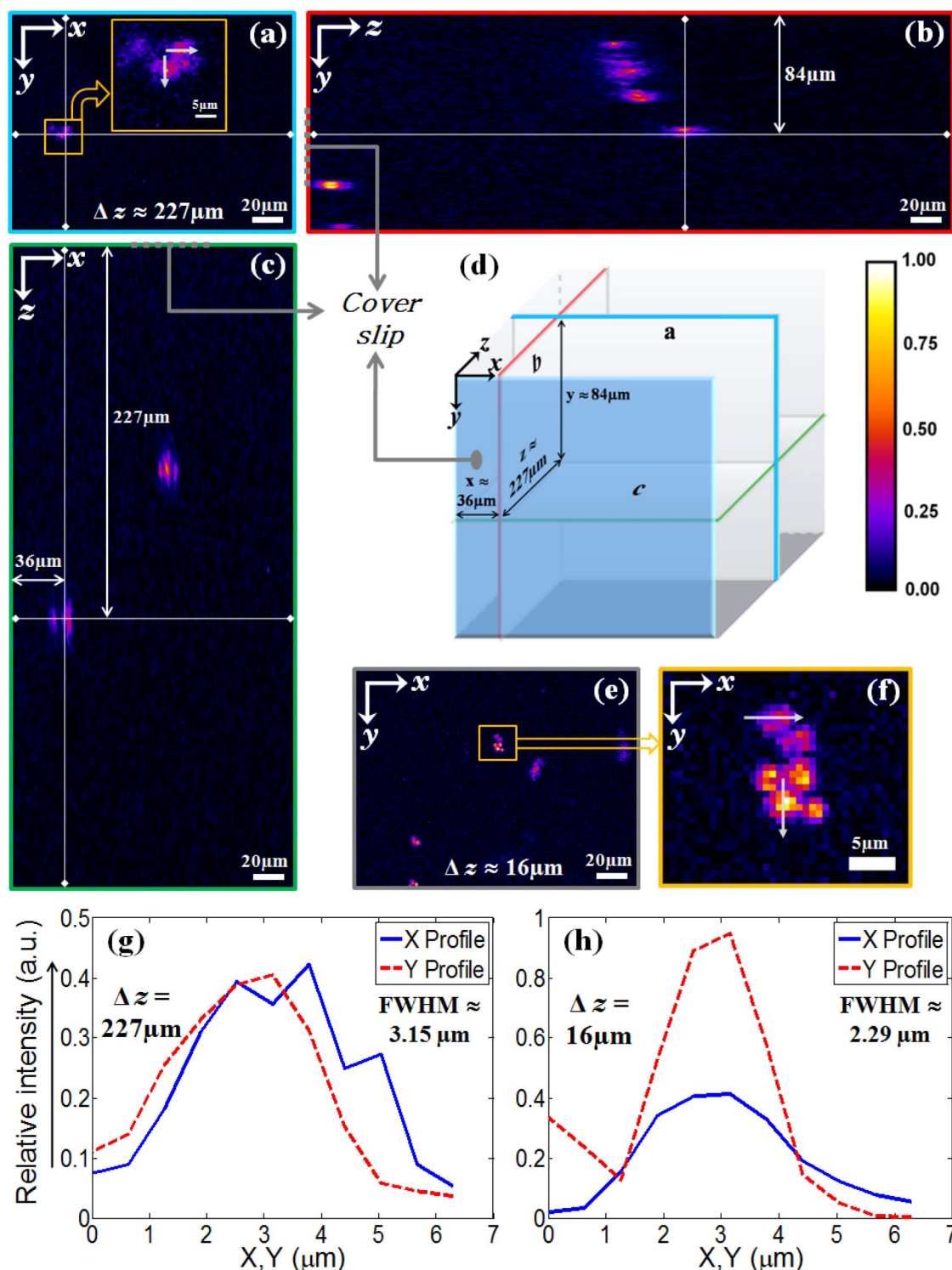


Figure 10 | The gel-matrix containing yeast cells (coated with multiple layers of polymer [PAH] conjugated with fluorescent dye [NHS-Rhodamin] and PSS), is imaged by using a confocal microscopy. Several XY images were acquired to form a 3D stack. The farthest observable yeast cell cluster was observed at a distance of $\Delta z = 227 \mu\text{m}$ from the sample boundary. (a) XY-plane of the 3D stack at a depth of $\Delta z = 227 \mu\text{m}$. The insert shows the zoomed portion of the Yeast cell cluster. (b) and (c) are the corresponding YZ and XZ planes, respectively, that are obtained from the 3D stack. (d) A schematic diagram depicting the location of the planes within the specimen and its distance from the coverslip. (e) For comparison, XY plane similar to (a) is also shown at a closer depth of $16 \mu\text{m}$. (f) Magnified view of a small Yeast cluster taken from the highlighted portion of (e). (g) and (h) are the intensity plots along the white lines in the inset figures of (a) and (f), respectively, for comparison at two varying depths. The broadening of the FWHM at a penetration depth of $227 \mu\text{m}$ is evident, indicating the deteriorating system resolution. Scale bars are inserted in the respective images.

tailored in the workshop to fine tune the edges. The back-aperture of the objective lens (Olympus, UPlanFLN 10X/0.3NA) is approximately 15 mm and the light is transmitted through the outermost window of $12 - 15 \text{ mm}$. The characteristics of the spatial filter mask are detailed in Supplementary 2. Upon excitation and with the consequent focusing by the excitation objective, the light from the periphery

undergoes constructive interference at the core along with low intensity rings due to further interferences.

To characterize the beam, we placed a CCD camera (Jenoptik MF_{conf}) directly at the geometrical focus of the illumination objective lens. The camera was then translated along the optical z -axis to collect the images of the XY-profile of the Bessel-like



beam. The translation was achieved using a micro-meter translator at an interval of 10 μm within a range of 1 mm. The images were then stacked together to obtain the 3D view of the field distribution as shown in figure 6.

We employed theta detection in which the light was collected 90° to the optical axis. The detection objective (Olympus, UPlanFLN 10X/0.3NA or Olympus UPlan FL 20X/0.4NA) collected and collimated the light. This was followed by an iris that is introduced to reduce spherical aberration. The fluorescence light was then allowed to pass through a biconvex lens (focal length 150 mm) that focuses it on the CCD camera. The data were collection from different z-layers of the specimen by translating the detection objective with incremental steps of 50 μm . To enable sharp focusing of the detection objective, the translator on which the sample was mounted was adjusted along the z-axis accordingly.

The sample chamber was mounted on a holder that was placed on two orthogonally oriented micrometer translation stages (Holmarc ,TS – 50 – Mu10 – 01, India). This arrangement allows the sample to be displaced with respect to the illuminating beam both axially (z-axis) and along the transverse x-axis with a resolution of 10 μm . We used cover-glass to build a sample chamber which ensured that we have a perfect parallel plane facing the illumination beam and the detection objective. Having an irregular surface facing the detection objective increases spherical aberration and as a result produces image distortion.

Sample preparation. Materials. Poly(styrenesulfonate sodium salt) (PSS; MW = 70,000), poly(allylamine hydrochloride) (PAH; MW = 15,000), Ammonium bicarbonate (NH_4HCO_3), calcium nitrate ($\text{Ca}(\text{NO}_3)_2$), Sodium chloride (NaCl) and dimethyl sulfoxide (DMSO) were obtained from Sigma- Aldrich. The fluorescent dye NHS-Rhodamine (MW: 528, Ex/Em wavelength: 552/575) and fluorescent dye removal columns were purchased from Thermo Scientific. Agar powder was acquired from Sd Fine Chemicals. An optical filter with a cutoff at 550 nm was purchased from Thorlabs for filtering the incident light.

System PSF characterization. To characterize the Bessel beam, we prepared a fluorescent gel sample. 100 mg of Agar powder was dissolved in 20 ml of distilled water and kept at 100°C for 10–15 min. The liquid gel was then allowed to cool down to 40°C. Then, 500 μlit of molten agar gel was added to 100 μlit of NHS-Rhodamine dye with constant stirring. This mixture was then poured into a detachable cubical chamber and allowed to solidify. Special care was taken to ensure that smooth surfaces faced the excitation light as well as the detection camera to reduce undue lensing effect. Once solidified, the fluorescent-gel sample was ready for the PSF characterization of the imaging system.

Preparation of the PAH-NHS rhodamine conjugate. The labeling procedure^{43,44} consisted of mixing a PAH solution (1 mg/ml) prepared in double-distilled water, with the dye dissolved in DMSO (10 mM), in a 1 : 15 (w : w) ratio. The mixture was then placed in the incubator. Darkness was maintained overnight with continuous gentle stirring to avoiding photobleaching. Subsequently, the resulting PAH-NHS Rhodamine was purified using fluorescent dye removal columns.

Coated yeast cell and CaCO_3 suspended gel samples. To prepare the gel sample, 100 mg of Agar powder was dissolved in 20 ml distilled water and heated at 100°C for 10 minutes. The melted agar gel was then cooled to 40°C. 500 μlit of melted agar gel is added to 100 μlit of coated CaCO_3 crystals with intense stirring. This was then shaped as a cube. The preparation of coated CaCO_3 is described in Supplementary I. Special care was taken to obtain a smooth surface that included the surface facing the excitation Bessel-like beam and the adjacent side facing the detection objective.

A similar technique was employed for preparing the Cell-suspended gel sample. Care was taken to cool the melted agar gel to 37°C. Then, 500 μlit of the gel solution was added to the coated yeast cells and mixed well by pipetting. The resulting mixture was then allowed to solidify in a cubical detachable container.

- Abbe, E. Note on the proper definition of the amplifying power of a lens or a lens system. *J. Roy. Microsc. Soc.* **4**, 348–351 (1884).
- Hell, S. W. & Stelzer, E. H. K. Fundamental improvement of resolution with a 4PI-confocal microscope using two-photon excitation. *Opt. Comm.* **93**, 277–282 (1992).
- Hell, S. W., Schmidt, R. & Egner, A. Diffraction-unlimited three-dimensional optical nanoscopy with opposing lenses. *Nature Photonics* **3**, 381–387 (2009).
- Hell, S. W. & Wichmann, J. Breaking the diffraction resolution limit by stimulated emission. *Opt. Lett.* **19**, 780–782 (1994).
- Hell, S. W. Far-field optical nanoscopy. *Science* **316**, 1153 (2007).
- Mondal, P. P. & Diaspro, A. Simultaneous multilayer scanning and detection for multiphoton fluorescence microscopy. *Sci. Rep.* **1**, 149 (2011).
- Mondal, P. P. Multi-focal multiphoton excitation fluorescence microscopy. *Rev. Sci. Instrum.* **80**, 096104 (2009).
- Gustafsson, M. G. L. Nonlinear structured-illumination microscopy: Wide-field fluorescence imaging with theoretically unlimited resolution. *PNAS USA* **102**, 13081–13086 (2005).
- Heintzmann, R., Jovin, T. & Cremer, C. Saturated patterned excitation microscopy concept for optical resolution improvement. *J. Opt. Soc. Am. A* **19**, 1599–1609 (2002).
- Chung, E., Kim, D. & So, P. T. C. Extended resolution wide-field optical imaging: objective-launched standing-wave total internal reflection fluorescence microscopy. *Opt. Lett.* **31**, 945–947 (2006).
- Francia, G. T. Super-gain antennas and optical resolving power. *Nuovo Cimento* **9**, 426–438 (1952).
- Botcherby, E. J., Juskaitis, R. & Wilson, T. Scanning two photon fluorescence microscopy with extended depth of field. *Opt. Comm.* **268**, 253–260 (2006).
- Betzig, E. *et al.* Imaging Intracellular Fluorescent Proteins at Nanometer Resolution. *Science* **313**, 1642–1645 (2006).
- Rust, M. J., Bates, M. & Zhuang, X. Sub-diffraction-limit imaging by stochastic optical reconstruction microscopy (STORM). *Nature Meth.* **3**, 793–795 (2006).
- Hess, S. T., Girirajan, T. P. K. & Mason, M. D. Ultra-high resolution imaging by fluorescence photoactivation localization microscopy. *Biophys. J.* **91**, 4258–4272 (2006).
- Fölling, J. *et al.* Fluorescence nanoscopy by ground-state depletion and single-molecule return. *Nature Methods* **5**, 943–945 (2008).
- Zanacchi, F. C. *et al.* Live-cell 3D super-resolution imaging in thick biological samples. *Nature Methods* **8**, 10471049 (2011).
- Axelrod, D., Burghardt, T. P. & Thompson, N. L. Total internal reflection fluorescence. *Ann. Rev. Biophys. Bioeng.* **13**, 247–268 (1984).
- Axelrod, D. Total internal reflection fluorescence microscopy in cell biology. *Meth. Enzymol.* **361**, 1–33 (2003).
- Mertz, J. & Kim, J. Scanning light-sheet microscopy in the whole mouse brain with HiLo background rejection. *J. Biomed. Opt.* **15**, 016027 (2010).
- Mondal, P. P., Vicidomini, G. & Diaspro, A. Markov Random Field Aided Bayesian Approach for Image Reconstruction in confocal microscopy. *TTT. Appl. Phys.* **102**, 044701 (2007).
- Mondal, P. P., Vicidomini, G. & Diaspro, A. Image reconstruction for multi-photon fluorescence microscopy. *Appl. Phys. Lett.* **92**, 103902 (2008).
- Schrader, M., Hell, S. W. & Van der Voort, H. T. M. Three-dimensional superresolution with a 4PI confocal microscope using image restoration. *Jl. Appl. Phys.* **18**, 4033 (1998).
- Wang, C. J., Carlton, P. M., Golubovskaya, I. N. & Cande, W. Z. Interlock formation and coiling of meiotic chromosome axes during synapsis. *Genetics* **183**, 905915 (2009).
- Greenfield, D. *et al.* Self-organization of the Escherichia coli chemotaxis network imaged with superresolution light microscopy. *PLoS Biol.* **7**, 6 (2009).
- Harata, N. C., Aravanis, A. M. & Tsien, R. W. Kiss-and-run and full-collapse fusion as modes of exo-endocytosis in neurosecretion. *J. Neurochem.* **97**, 154615470 (2006).
- Taraska, J. W., Perrais, D., Ohara-Imaizumi, M., Nagamatsu, S. & Almers, W. Secretory granules are recaptured largely intact after stimulated exocytosis in cultured endocrine cells. *Proc. Natl. Acad. Sci. USA* **100**, 20702075 (2003).
- Merrifield, C. J., Feldman, M. E., Wan, L. & Almers, W. Imaging actin and dynamin recruitment during invagination of single clathrin-coated pits. *Nat. Cell Biol.* **4**, 691698 (2002).
- Grotjohann, T. *et al.* Diffraction-unlimited all-optical imaging and writing with a photochromic GFP. *Nature* **478**, 204–208 (2011).
- Schmidt, R. *et al.* Spherical nanosized focal spot unravels the interior of cells. *Nat. Methods* **5**, 539544 (2008).
- Schermelleh, L. *et al.* Subdiffraction multicolor imaging of the nuclear periphery with 3D structured illumination microscopy. *Science* **320**, 13321336 (2008).
- Planchon, T. A. *et al.* Rapid three-dimensional isotropic imaging of living cells using Bessel beam plane illumination. *Nature Methods* **8**, 417423 (2011).
- Voie, A. H., Burns, D. H. & Spelman, F. A. Orthogonal-plane fluorescence optical sectioning: three-dimensional imaging of macroscopic biological specimens. *J. Microsc.* **170**, 229236 (1993).
- Huiskens, J., Swoger, J., Del Bene, F., Wittbrodt, J. & Stelzer, E. H. K. Optical sectioning deep inside live embryos by selective plane illumination microscopy. *Science* **305**, 1007–1009 (2004).
- Mondal, P. P. & Diaspro, A. Lateral resolution improvement in two-photon excitation microscopy by aperture engineering. *Opt. Comm.* **281**, 1855–1859 (2008).
- Wang, H., Shi, L., Lukyanchuk, B., Sheppard, C. & Chong, C. T. Creation of a needle of longitudinally polarized light in vacuum using binary optics. *Nature Photonics* **2**, 501–505 (2008).
- Mondal, P. P., Mandal, S. & Diaspro, A. Dynamic point spread function for single and multiphoton fluorescence microscopy. *Rev. Sci. Instrum.* **81**, 046103 (2010).
- Denk, W., Strickler, J. H. & Webb, W. W. Two-photon laser scanning fluorescence microscopy. *Science* **248**, 73–76 (1990).
- Bouchal, Z., Wagner, J. & Chlup, M. Self-reconstruction of a distorted nondiffracting beam. *Opt. Commun.* **151**, 207–211 (1998).
- Miller CE, Thompson RP, Bigelow MR, Gittinger G, Trusk TC, Sedmera D. Confocal imaging of the embryonic heart: how deep? *Microsc Microanal.* **11**, 216–223 (2005).
- Wolf, E. & Richards, B. Electromagnetic diffraction in optical systems II. Structure of the image field in an aplanatic system. *Proc. Roy. Soc. A* **253**, 358–379 (1959).
- Boivin, A. & Wolf, E. Electromagnetic field in the neighborhood of the focus of a coherent beam, *Phys. Rev.* **138**, B1561–B1565 (1965).
- Yang, W., Trau, D., Renneberg, R., Yu, N. T. & Caruso, F. J. Layer-by-Layer Construction of Novel Biofunctional Fluorescent Microparticles for Immunoassay Applications. *Colloid Interface Sci.* **234**, 356–362 (2001).



44. Hermanson, G. T. *Bioconjugate Techniques*. Academic Press: London, Chapter 8, pp 303–305 (1996).

Acknowledgements

PPM would like to acknowledge BRNS (DAE), DST and the parent institute (Indian Institute of Science) for financial support.

Author contributions

PPM and SBP conceived and designed the study. SBP and PPM performed the experiments whereas, computational studies were carried out by SBP. The samples were prepared by SB. SBP and PPM analyzed the data and produced the figures. PPM and SBP wrote the manuscript.

Additional information

Supplementary information accompanies this paper at <http://www.nature.com/scientificreports>

Competing financial interests: The authors declare no competing financial interests.

License: This work is licensed under a Creative Commons Attribution-NonCommercial-ShareAlike 3.0 Unported License. To view a copy of this license, visit <http://creativecommons.org/licenses/by-nc-sa/3.0/>

How to cite this article: Purnapatra, S.B., Bera, S. & Mondal, P.P. Spatial Filter Based Bessel-Like Beam for Improved Penetration Depth Imaging in Fluorescence Microscopy. *Sci. Rep.* 2, 692; DOI:10.1038/srep00692 (2012).